Aerosol and Cloud Interaction Observed from High Spectral Resolution Lidar Data

Wenying Su,

Science Systems and Applications Inc., Hampton, VA, USA

Gregory L. Schuster, Norman G. Loeb,

NASA Langley Research Center, Hampton, VA, USA

Raymond R. Rogers,

Science Systems and Applications Inc., Hampton, VA, USA

Richard A. Ferrare, Chris A. Hostetler, Johnathan W. Hair

NASA Langley Research Center, Hampton, VA, USA

Michael D. Obland

Science Systems and Applications Inc., Hampton, VA, USA

W. Su, Science Systems and Applications Inc., MS420, NASA Langley Research Center, Hampton, VA 23681, USA. (Wenying.Su-1@nasa.gov)

Abstract. Recent studies utilizing satellite retrievals have shown a strong correlation between aerosol optical depth (AOD) and cloud cover. However, these retrievals from passive sensors are subject to many limitations, including cloud adjacency (or 3D) effects, possible cloud contamination, uncertainty in the AOD retrieval. Some of these limitations do not exist in High Spectral Resolution Lidar (HSRL) observations; for instance, HSRL observations are not affected by cloud adjacency effects, are less prone to cloud contamination, and offer accurate aerosol property measurements (backscatter coefficient, extinction coefficient, lidar ratio, backscatter Angstrom exponent, and aerosol optical depth) at a fine spatial resolution (< 100 m) in the vicinity of clouds. Hence, the HSRL provides an important dataset for studying aerosol and cloud interaction.

In this study, we statistically analyze aircraft-based HSRL profiles according to their distance from the nearest cloud, assuring that all profile comparisons are subject to the same large-scale meteorological conditions. Our results indicate that AODs from HSRL are about 8∼17% higher in the proximity of clouds (∼100 m) than far away from clouds (4.5 km), which is much smaller than the reported cloud 3D effect on AOD retrievals. The backscatter and extinction coefficients also systematically increase in the vicinity of clouds, which can be explained by aerosol swelling in the high relative humidity (RH) environment and/or aerosol growth through in cloud processing (albeit not conclusively). On the other hand, we do not observe a systematic trend in lidar ratio; we hypothesize that this is caused by the op-

posite effects of aerosol swelling and aerosol in-cloud processing on the lidar ratio. Finally, the observed backscatter Angstrom exponent (BAE) does not show a consistent trend because of the complicated relationship between BAE and RH. We demonstrate that BAE should not be used as a surrogate for Angstrom exponent, especially at high RH.

1. Introduction

Several satellite studies indicate that regions with increased cloud cover are accompanied by increased aerosol optical depths (AODs) in the clear areas between the clouds, and that this phenomenon is occurring globally [*Sekiguchi et al.*, 2003; *Ignatov et al.*, 2005; *Loeb and Manalo-Smith*, 2005; *Kaufman et al.*, 2005; *Matheson et al.*, 2005, 2006; *Loeb and Schuster*, 2008] . Possible explanations for this observed trend include cloud contamination in the aerosol retrieval, aerosol swelling in the high-humidity cloudy environments [*Clarke et al.*, 2002], increased illumination of the cloud-free columns by the nearby clouds (i.e., the cloud adjacency or 3D effect) [*Podgorny*, 2003; *Wen et al.*, 2006, 2007], increased particle production in the vicinity of clouds [*Hegg et al.*, 1990; *Hoppel et al.*, 1994; *Clarke et al.*, 1998], and shift of aerosol size distribution to larger size because of cloud processing and cloud evaporation in the vicinity of clouds [*Lelieveld and Heintzenberg*, 1992; *Alkezweeny*, 1995; *Hegg et al.*, 2004].

Wen et al. [2006, 2007] studied the 3D cloud radiative effects on MODIS aerosol retrievals over Brazil. Their Monte Carlo simulations indicate that ignoring the cloud adjacency effect can cause an overestimation of 50 to 140% in AOD retrieval, with the overestimation more pronounced at shorter wavelengths. Larger increase of AOD at shorter wavelengths is also shown in stochastic cloud model simulations [*Marshak et al.*, 2008]. They argue that the enhancement in the cloud-free column radiance comes from the enhanced Rayleigh scattering.

In this study, we examine the aerosol properties both in the vicinity of clouds and far away from clouds using nadir-viewing aircraft-based High Spectral Resolution Lidar

(HSRL) profiles of aerosol backscatter and extinction coefficients. The HSRL has many advantages over passive satellite instruments for observing aerosol and cloud interactions, including: 1.) it provides accurate measurements of aerosol properties in the vicinity of clouds as opposed to the aerosol *retrievals* provided by satellites; 2.) it is an active instrument with a narrow source, so it is not affected by cloud adjacency effects; 3.) the backscatter coefficient of cloud droplets is much larger than that of aerosols, so cloud boundaries are readily distinguishable; and 4.) the HSRL has a spatial resolution of $<$ 100 m, which makes the clear profiles less prone to cloud contamination than the much larger clear pixels ($\geq$500 m) associated with satellite instruments. But the disadvantage of HSRL measurement is that it has limited spatial coverage and can only provide cloud top height along the flight track.

2. Method

A standard backscatter lidar measures attenuated backscatter; retrieving extinction profiles from a backscatter lidar requires the assumption of extinction-to-backscatter ratio (i.e., lidar ratio). Unfortunately, the actual value of lidar ratio for tropospheric aerosols can vary over a wide range (from 20 to 100 sr) depending on their optical properties [*Ansmann et al.*, 1990; *Ackermann*, 1998; *Anderson et al.*, 2000; *Ferrare et al.*, 2001; *Cattrall et al.*, 2005], which leads to large uncertainty in the retrieved aerosol extinction. Unlike a standard backscatter lidar, the HSRL provides measurements of both aerosol extinction and backscatter, which enables the robust computation of the lidar ratio.

In this section, first we describe the NASA Langley Research Center (LaRC) airborne HSRL, then we describe our statistical analysis of HSRL data. We compare each HSRL clear profile to a clear profile next to clouds (i.e., reference profile); this analysis method

ensures that both the clear profile and the reference profile are subject to the same large-scale meteorological conditions. For a given flight, aerosol properties of all clear profiles and differences between clear profiles and reference profiles are binned by clear profiles' distances to the nearest clouds. For each bin, average differences are presented and possible causes for the differences are analyzed.

2.1. Description of LaRC HSRL

The LaRC HSRL instrument and its measurement technique is described in *Hair et al.* [2006], which we briefly review here. The basic concept of HSRL measurements is to obtain the lidar return signal with high spectral resolution (< 75 MHz laser bandwidth), which enables the separation of aerosol and cloud returns from molecular returns. This separation is possible because the spectrum of the molecular backscatter is Doppler broadened by the thermal motion of the molecules, whereas Doppler broadening of the aerosol and cloud backscatter is negligible because of the much slower thermal velocities of the aerosol/cloud particles. The separation of molecular from aerosol/cloud backscatter enables the independent retrieval of aerosol/cloud backscatter and extinction profiles. Another key feature of the LaRC HSRL is the ability to calibrate the instrument internally, thereby eliminating systematic errors associated with vicarious calibration in regions that are assumed to have negligible aerosol loading.

The LaRC HSRL includes three measurement channels at the 532 nm wavelength and two measurement channels at the 1064 nm wavelength; parallel and perpendicular scattering channels are included at both wavelengths, and an additional channel for molecular scattering is included at the 532 nm wavelength. The molecular channel makes it possible to derive reliable aerosol backscatter (β) and extinction (σ) profiles at 532 nm, and hence

the aerosol lidar ratio: $S_a = \sigma/\beta$. A lidar ratio is assumed to derive extinction profiles for the 1064 nm wavelength (although a more sophisticated algorithm incorporating the 532 nm lidar ratio could be implemented in the future).

Two additional parameters can be derived from the HSRL measurements. The aerosol depolarization ratio can be calculated from the perpendicular and parallel backscatter at both wavelengths: $\delta = \beta^{\perp}/\beta^{\parallel}$. We also define the backscatter Angstrom exponent (BAE, analogous to the Angstrom exponent):

$$BAE = \frac{-\ln(\beta_{1064}/\beta_{532})}{\ln(2)}, \quad (1)$$

where the denominator represents the logarithm of the wavelength ratio. The absolute uncertainties of these HSRL observed variables used in this study are listed in Table 1.

2.2. Statistical Analysis Method

The LaRC HSRL was deployed on the LaRC's King Air B-200 aircraft during the CATZ [1] campaign over the Eastern United States (June 26 to August 29, 2007). One of the objectives of this campaign was to investigate the nature of particles in the 'twilight zone' between clouds and aerosols [*Koren et al.*, 2007]. The aircraft flew at an altitude of 9 km, and measurements were averaged over 100 shots (0.5 sec) in the lidar electronics before being transferred to a laptop computer. Within 0.5 sec, HSRL usually covers a spatial resolution of 50–75 m, depending upon the flight speed of the aircraft (which varies somewhat during each flight). The vertical resolution of backscatter and extinction are 30 m and 300 m, respectively.

[1] CALIPSO (Cloud-Aerosol Lidar and Infrared Pathfinder Satellite Observation) AERONET (Aerosol Robotic Network) Twilight Zone

As our objective is to understand changes in aerosol optical properties in the vicinity of boundary layer clouds, we must first determine the proximity of the lidar beam to a cloud boundary. We identify cloud top altitudes for clouds located at or near the top of the planetary boundary layer using background subtracted, range-square-corrected profiles from the HSRL. A three point Haar wavelet covariance transform [*Gamage and Hagelberg*, 1993] is used to detect the sharp gradients in these HSRL profiles associated with cloud boundaries.

Thus, the location of clouds along the flight track can be easily determined using HSRL data, but the HSRL cannot provide information about clouds that are not directly underneath the aircraft. The ideal flight tracks for our aerosol and cloud interaction study are those that have almost no clouds on either side of the clear portions on the tracks. We visually inspected Geostationary Operational Environmental Satellites (GOES) images obtained during the CATZ campaign to identify those ideal cases, and chose segments of flights on August 4^{th}, 7^{th}, and 9^{th} for our study. Note the spatial resolution of GOES visible images is 1 km; therefore subpixel clouds may still be nearby. Backscatter profiles of the time periods used in this analysis for the three days are shown in Fig. 1. The August 4^{th} flight segment covers a distance of about 250 km from Maryland to Virginia with AOD around 0.4, the August 7^{th} flight segment covers a distance of about 560 km off the coast of North Carolina with AOD around 0.7, and the August 9^{th} flight segment covers a distance of about 200 km off the coast of South Carolina with AOD around 0.9.

Next, we choose a reference altitude of the low clouds (H_c) for each flight segment (H_c = 2000 m, 500 m, and 500 m for August 4^{th}, 7^{th}, and 9^{th}, respectively), and analyze all of the clear HSRL profiles at this altitude. We define a profile as being 'clear' if it does

not have a valid cloud top height but has valid backscatter and extinction measurements over the entire altitude range. We define a profile as being 'cloudy' if it has a valid cloud top height between H_c and $H_c + 200$ m, assuming that the geometrical thickness of the boundary layer clouds is about 200 m [*Bennartz*, 2007]. However, we also tested cloud geometrical thickness of 500 m and 1000 m, which did not change the general trends of our results.

Then we save the aerosol optical properties $(\beta, \sigma, S_a, BAE)$ in each clear profile (x_i), and search the temporal record to identify the closest cloudy profile (x_j) that occurs before or after x_i. Since x_j is the nearest cloudy profile, any profile (such as x_{j+1} and x_{j+2}) between it and x_i is clear. We are interested in how aerosol properties in the near-cloud environment differ from the aerosol properties in the far-cloud environment, so we also note the aerosol optical properties in a clear profile x_{j+2}, which is $\sim$100 m from x_j. Hereafter, x_{j+2} is referred to as reference profile. We choose x_{j+2} instead of x_{j+1} to reduce the possibility of cloud contamination that could occur in profiles that are too close to clouds (x_{j+1} is about $\sim$50 m away from x_j). Nonetheless, our analysis produces statistically equivalent results when using x_{j+1} or x_{j+2} for the near-cloud reference profile, which is a testament to the robustness of the cloud screening technique used for the HSRL data.

We calculate the difference in aerosol optical properties between profile x_i and reference profile x_{j+2} (for example, $\delta\beta = \beta_i - \beta_{j+2}$, where β_{j+2} is the near-cloud reference value) and the difference is binned according to the distance between x_i and x_j. Here we consider seven bins, which are listed in Table 2, along with the total number of samples in each

bin for the three days analyzed in this study. For each bin, the averaged difference $(\overline{\delta\beta}, \overline{\delta\sigma}, \overline{\delta S_a}, \overline{\delta BAE})$ and the standard error for each aerosol property are calculated.

3. Results

Figure 2 shows the averaged differences for 532 nm backscatter coefficient ($\overline{\delta\beta}$, in unit $Mm^{-1}sr^{-1}$) for the three days. The averaged near-cloud reference backscatter coefficients ($\overline{\beta_{j+2}}$) are also included. The error bars for each bin in Figure 2 are given by the standard error of that bin, calculated as the standard deviation of the differences divided by the square root of the number of samples of that bin. Figure 2 indicates systematic increases in β as clear profiles get closer to clouds. For example, on August 4^{th}, $\overline{\beta_{j+2}}$ is about 1.2 $Mm^{-1}sr^{-1}$ (23%) higher than the averaged backscatter coefficient in the second distance bin (501–1000 m away from nearest clouds); and $\overline{\beta_{j+2}}$ is about 1.4 $Mm^{-1}sr^{-1}$ (27%) higher than the averaged backscatter coefficient in the seventh distance bin (4001–5000 m away from nearest clouds). The other two days show similar increasing trends of β as the clear profiles get closer to clouds. $\overline{\beta_{j+2}}$ is about 30% and 26% higher than the averaged backscatter coefficient in the seventh bin for August 7^{th} and 9^{th}.

The uncertainty of the averaged difference in each bin associated with the instrumental error can be calculated by dividing the instantaneous uncertainty, listed in Table 1, by the square root of the total number of samples of that bin. For example, the instrumental error in $\overline{\delta\beta}$ is about 0.06 $Mm^{-1}sr^{-1}$ for the first bin on August 4^{th}. The $\overline{\delta\beta}$ shown in Figure 2 is much larger than the instrumental error for all the bins on the three days, which indicates that the systematic trend is not affected by random instrumental error.

Depolarization ratios at 532 nm during these three days are less than 0.02 and exhibit nearly no changes in the vicinity of clouds, indicating that there are very few non-spherical dust particles.

The extinction coefficients at 532 nm for the three days are qualitatively similar to backscatter coefficients (figure not shown). For clear profiles in the second bin, the averaged extinction coefficients are about 0.10, 0.06, and 0.10 km^{-1} lower than those near-cloud reference values and correspond to 24%, 10%, and 13% decreases. The differences are 0.17, 0.10, and 0.17 km^{-1} for clear profiles in the seventh bin and correspond to 42%, 17%, and 23% decreases. Again, the averaged extinction differences in all bins for the three days are much larger than the instrumental errors.

Aerosol optical depth (AOD) can be computed by integrating the HSRL measured extinction profiles between the surface and the flight altitude of 6.5 km. Differences between AODs that are near and far from clouds are analyzed using the same method. Figure 3 shows the averaged differences for AOD at 532 nm ($\overline{\delta AOD}$). Averaged near-cloud reference AODs are also listed. AODs from profiles in the second distance bin are 0.03, 0.02 and 0.07 lower than those near-cloud reference values, on August 4^{th}, 7^{th}, and 9^{th}, respectively. These correspond to 6%, 3%, and 8% decreases relative to the reference AODs. AODs from profiles in the seventh distance bin are 0.04, 0.06, and 0.16 (9%, 8%, and 17%) lower than the near-cloud reference AODs. The averaged AOD differences in all bins for the three days are much larger than the instrumental errors.

Figure 4 shows the averaged differences for the 532 nm lidar ratio ($\overline{\delta S_a}$) for the three days. Unlike the systematic decreases seen in β, σ, and AOD as clear profiles get farther away from clouds, we do not see any consistent changes in $\overline{\delta S_a}$ (except for those between

2000 and 5000 m away from the nearest clouds on August 4^{th}). Note the instrumental error in $\overline{\delta S_a}$ for some bins with small number of samples can be up to 3 sr, which could be responsible for some of the variability seen in Figure 4. We also notice that the averaged near-cloud reference lidar ratios are $\sim$ 80 sr for the three days that we investigated. Since the lidar ratio for water clouds is significantly lower ($\sim$ 18 sr) [*Pinnick et al.*, 1983; *O'Connor et al.*, 2004], this once again shows that our results are not affected by significant cloud contamination.

Figure 5 shows the averaged differences for the BAE, and the averaged near-cloud reference BAEs. The trends of BAE are mixed. On August 4^{th}, no systematic changes of BAEs are observed within 1500 m of clouds. Thereafter the BAEs decrease by about 0.05 to 0.14 (5% to 13% relative to the near-cloud value) as the clear profiles get farther away from the nearest clouds. On August 7^{th}, BAEs exhibit systematic increases as the clear profiles move farther away from clouds. BAEs increase by about 0.15 to 0.09 (12% to 8 %) for clear profiles that are between 2000 and 5000 m away from the nearest clouds. On August 9^{th}, there is no systematic changes in BAEs.

4. Discussion

The increased backscatter and extinction coefficients observed with the HSRL in the vicinity of clouds are not caused by cloud adjacency effects or cloud contamination; we know this because of the advantages of HSRL measurements outlined in Section 1 (i.e., narrow field of view and high sensitiviy to differences in scattering caused by aerosols and cloud drops). Other possible causes include: 1.) new particle production in the vicinity of clouds; 2.) aerosol growth through in-cloud aqueous oxidation of SO_2 to sulfate and

collision/coalescence; and 3.) aerosol swelling as relative humidity (RH) increases near clouds.

New particle production in the vicinity of clouds alters the aerosol size distribution. *Hegg et al.* [1990] noted that aerosol number size distribution in the vicinity of clouds consists of more smaller particles ($r < 0.05\mu m$) than the nearby clear air aerosol size distribution, and suggested that this is due to homogeneous heteromolecular nucleation. *Hoppel et al.* [1994] observed a large number of small particles ($r < 0.01\mu m$) above the cloud top and interpreted this as an evidence of new particle formation. *Clarke et al.* [1998] also observed significant increase of ultra fine particles ($0.002 < r < 0.005\mu m$) at the edges of clouds. However, given the very small size of these particles, they are unlikely to affect the measured extinction and backscatter coefficients [*Schuster et al.*, 2006].

Aerosol growth near clouds has been observed in both *in situ* measurements and model simulations. *Alkezweeny* [1995] measured a decreased aerosol number concentration for optically active aerosols with radii below 0.2 μm, and an increased aerosol number concentration for aerosol radii between 0.2 and 1.5 μm in the processed clear air. He argued that the in-cloud chemical conversion of SO_2 to sulfate adds new material to droplet. Since every droplet generates only one aerosol particle upon evaporation [*Mitra et al.*, 1992], the new size is therefore larger. Although *Alkezweeny* [1995] did not measure particle sizes greater than 1.5 μm, we note that the increase in particle number concentrations altered the particle size distribution of the coarse mode ($r \gtrsim 0.5\,\mu$m) as well as the accumulation mode.

Hegg et al. [2004] observed enhanced light-scattering efficiency in the vicinity of clouds, and attributed the enhancement to a shift in the aerosol size distribution toward a more

effective scattering size range. *Feingold and Kreidenweis* [2002] used a large eddy simulation to demonstrate that aqueous chemistry increased the aerosol number concentration for radii between 0.1 and 1.5 μm (no data were shown beyond 1.5 μm). *Kerkweg et al.* [2003] used an air-parcel model to demonstrate that aqueous chemistry and coalescence of cloud droplets enhanced the number of larger aerosol particles ($r > 2\,\mu m$) in the processed aerosol size distribution.

Swelling of aerosols in the high RH environment can alter their optical properties and possibly their size distribution depending on their composition. We investigate the observed near- and far-cloud differences in aerosol optical properties by simulating aerosol hygroscopic growth, following the method outlined in *Loeb and Schuster* [2008]. That is, we assume that the aerosols in our study are an equilibrium mixture [*Tang*, 1996] of ammonium sulfate and water in the fine mode and sea salt (or dust) in the coarse mode, and that the size distribution is represented by the GSFC climatology of *Dubovik et al.* [2002]. Then we use Mie theory [*Wiscombe*, 1980] to compute the backscatter, extinction, lidar ratio, and backscatter Angstrom exponent.

The backscatter coefficient (β) and lidar ratio (S_a) are plotted in Figures 6 and 7 at four dry fine volume fractions, assuming sea salt occupies the coarse mode. The results for dust in the coarse mode are qualitatively similar, except that the sensitivity of the lidar ratio to dry fine volume fraction is smaller at high RH. Since the hygroscopic growth factor is different for the fine and coarse modes in our simulations (owing to the different composition of the two modes), the *wet* fine volume fraction changes along the curves in Figures 6 and 7, even though the *dry* fine volume fraction remains the same. Hereafter, all fine volume fractions in our discussion refer to dry fine volume fractions. If aerosol

swelling in the vicinity of clouds is the only mechanism altering the β and S_a, the aerosol properties are expected to follow a single curve. However, if aerosol growth through in-cloud processing alters the relative distribution of the fine and coarse modes, then β and S_a will move from one curve to another in Figures 6 and 7.

Figure 6 shows the simulated backscatter coefficient (β) as a function of RH for four dry fine volume fractions; β increases by a factor of two as RH increases from 55% to 90%, and thereafter it increases sharply. In fact, β at 99% RH is more than an order of magnitude larger than at 55% RH. Also note that β is not sensitive to fine volume fraction for RH less than 97%, especially for aerosols dominated by the fine mode (like pollution). The relationship between extinction coefficient and RH is qualitatively similar to our backscatter coefficient simulation (figure not shown); the extinction coefficient is also not sensitive to the fine volume fraction when RH is less than 97%.

Figure 6 clearly indicates that aerosol swelling is consistent with the unambiguous increase of backscatter and extinction coefficients observed in the vicinity of clouds (Figure 2). In addition, aerosol growth through in-cloud processing (which enhances the aerosol light-scattering efficiency), can also increase backscatter and extinction in the vicinity of clouds.

The unambiguous increase of extinction coefficients also translates to the increase of column aerosol optical depths at 532 nm in the vicinity of clouds. AODs increase by about 8% to 17% in the vicinity of clouds than far away from clouds (4.5 km). *Koren et al.* [2007] found that AOD at 440 nm decreased by about 13%$\pm$2% on average from the first sample measured near a cloud to the second sample (less than 15 minutes later). In their study, multiple years of data from 15 AERONET stations were used, and the boundary

layer wind speed data were not always available at these stations to translate the time interval between these two samples to geometrical distance. However, if we assume a boundary layer wind speed of 4.96 $m\,s^{-1}$ [the globally averaged daytime 80-m wind speed from *Archer and Jacobson*, 2005], we can approximate the distance between these two samples to be $\sim$ 4.5 km. Although the wind speed we use here is a crude approximation, it nonetheless shows that AOD increases in the vicinity of clouds at nearly the same magnitude for both the *Koren et al.* [2007] study and our study. The AOD increase in the vicinity of clouds from these two studies (which are not affected by cloud adjacency effects) is much smaller than the cloud adjacency effects on AOD retrieval (50 to 140% overestimation) [*Wen et al.*, 2006, 2007].

The simulated lidar ratio (S_a) also increases as dry fine volume fraction and RH increase, as shown in Figure 7. If aerosol swelling is the only mechanism affecting our HSRL measurements in the vicinity of clouds, then S_a should increase near clouds, which is not consistent with our observations; two out of three days shown in Figure 4 do not exhibit any systematic trend in S_a. One possible explanation is aerosol growth caused by oxidation of SO_2 and collision/coalescence increases the relative fraction of coarse mode aerosols in the vicinity of clouds. Since S_a is smaller for coarse mode aerosols than for fine mode aerosols, this counteracts the enhancement in S_a caused by aerosol swelling; hence, the non-systematic trend in Figure 4. Unfortunately, we do not have simultaneous aerosol size and RH measurements to verify this hypothesis.

The simulated BAE increases as fine volume fraction at a given RH (as expected), but the relationship between RH and BAE is not monotonic (figure not shown). BAE first decreases as RH increases, until a certain RH (96% and 90%, respectively, for fine volume

316 fraction of 0.3 and 1), then BAE increases. Therefore, depending on the RH values next
317 to clouds and away from clouds, and the aerosol properties along the flight tracks, the
318 BAE differences shown in Figure 5 can be explained by aerosol swelling and growth. This
319 once again stresses the importance of concurrent RH and aerosol property measurements.

320 To investigate if BAE could be used as a surrogate for Angstrom exponent (AE), we
321 present BAE as a function of AE for four dry fine volume fractions as RH increases
322 from 55% to 99% in Figure 8, using sea salt for the coarse mode. The AE is defined for
323 wavelengths 553 and 855 nm, which are the same wavelengths used for one of the MODIS'
324 AEs over the ocean [*Remer et al.*, 2005]. For RH less than ~85%, BAE and AE are linearly
325 correlated for aerosol size distributions dominated by the fine mode (BAE decreases as
326 AE decreases). As aerosols continue to swell, however, the BAE increases while the AE
327 decreases. Also, the BAE and AE are anti-correlated for coarse mode dominated aerosols
328 over the RH range considered here. Therefore, the humidification trends of BAE and AE
329 are not similar, and BAE should not be used as a surrogate for Angstrom exponent. Also,
330 the information content about the aerosol size distribution in the BAE is very limited, as
331 also shown by *Feingold and Grund* [1994].

5. Summary

332 We used aircraft HSRL measurements to study aerosol and cloud interaction during the
333 CATZ campaign. Unlike satellite retrievals, HSRL observations are not affected by cloud
334 adjacency effects, and offer accurate measurements of aerosol properties in the vicinity of
335 clouds. (The aerosol properties investigated in this study include aerosol backscatter and
336 extinction coefficients, lidar ratios, backscatter Angstrom exponents, and column aerosol
337 optical depths.) The HSRL also provides robust cloud screening, and we used GOES

images to select observational periods with very few low clouds on both sides of the flight tracks, thereby minimizing the effects of clouds that do not appear in the lidar beam.

We examined the aerosol properties of HSRL profiles in the vicinity of clouds according to the distance from the nearest clouds, observing differences between clear profiles that are adjacent to clouds (~100 m from clouds) and clear profiles that are up to 5000 m away from clouds. The short distance between these profiles (<5000 m) assures the same large-scale meteorological condition for both profiles, which is important for studying aerosol and cloud interactions [*Loeb and Manalo-Smith*, 2005; *Mauger and Norris*, 2007; *Loeb and Schuster*, 2008].

Results from three observations in August 2007 reveal unambiguous increases of backscatter coefficients, extinction coefficients, and aerosol optical depths in the vicinity of clouds. These increases are possibly caused by aerosol swelling and aerosol growth in the vicinity of clouds. However, we do not observe any systematic lidar ratio changes in the vicinity of clouds. We hypothesize that changes in S_a are neutralized by the opposite effects of aerosol swelling associated with a high relative humidity environment (which increases S_a), and aerosol growth associated with cloud processing (which decreases S_a if the aerosol size distribution shifts to the coarse mode). We do not observe systematic changes of BAE in the vicinity of clouds, either. Theoretical simulations reveal that the relationship between BAE and RH is rather complicated, and that it would be rather difficult to infer changes in the aerosol size distribution from BAE. Furthermore, BAE should not be used as a surrogate for Angstrom exponent, especially at high relative humidity.

Acknowledgments. The authors thank the support from NASA CALIPSO program and NASA Interdisciplinary Research in Earth Science under the direction of Dr. Hal

361 Maring. The authors are grateful to Bill Smith Jr. for discussions on GOES image. At
362 the time this research was performed, Michael Obland was a NASA postdoctoral fellow
363 at NASA Langley Research Center, administered by Oak Ridge Associated Universities
364 through a contract with NASA.

References

Ackermann, J. (1998), The extinction-to-backscatter ratio of tropospheric aerosol: a numberical study, *J. Atmos. Oceanic Technol.*, *15*, 1043–1050.

Alkezweeny, A. J. (1995), Field observations of in-cloud nucleation and the modification of atmospheric aerosol size distribution after cloud evaporation, *J. Appl. Meteor.*, *34*, 2649–2654.

Anderson, T. L., S. J. Masonis, D. S. Covert, R. J. Charlson, and M. J. Rood (2000), In situ measurement of the aerosol extinction-to-backscatter ratio at a polluted continental site, *J. Geophys. Res*, *105*(D22), 26,907–26,915.

Ansmann, A., M. Riebesell, and C. Weitkamp (1990), Measurement of atmospheric aerosol extinction profiles with a raman lidar, *Opt. Lett.*, *15*, 746–748.

Archer, C. L., and M. Z. Jacobson (2005), Evaluation of global wind power, *J. Geophys. Res*, *110*(D12110), doi:10.1029/2004JD005462.

Bennartz, R. (2007), Global assessment of marine boundary layer cloud droplet number concentration from satellite, *J. Geophys. Res*, *112*(D02201), doi:10.1029/2006JD007547.

Cattrall, C., J. Reagan, K. Thome, and O. Dubovik (2005), Variability of aerosol and spectral lidar and backscatter and extinction ratios of key aerosol types derived from selected aerosol robotic network locations, *J. Geophys. Res*, *110*(D10S11), doi: 10.1029/2004JD005124.

Clarke, A. D., J. L. Varner, F. Eisele, R. L. Mauldin, and D. Tanner (1998), Particle production in the remote marine atmosphere: Cloud outflow and subsidence during ace 1, *J. Geophys. Res*, *103*(D13), 16,397–16,409.

Clarke, A. D., S. Howell, P. K. Quinn, T. S. Bates, J. A. Ogren, and coauthors (2002), INDOEX aerosol: A comparison and summary of chemical, microphysical, and optical properties observed from land, ship, and aircraft, *J. Geophys. Res*, *107*(8033), doi: 10.1029/2001JD000572.

Dubovik, O., B. Holben, T. Eck, A. Smirnov, Y. Kaufman, M. King, D. Tanre, and I. Slutsker (2002), Variability of absorption and optical properties of key aerosol types observed in worldwide locations, *J. Atmos. Sci.*, *59*, 590–608.

Feingold, G., and C. J. Grund (1994), Feasibility of using multiwavelength lidar measurements to measure cloud condensation nuclei, *J. Atmos. Oceanic Technol.*, *11*, 1543–1558.

Feingold, G., and S. M. Kreidenweis (2002), Cloud processing of aerosol as modeled by a large eddy simulation with coupled microphysics and aquaous chemistry, *J. Geophys. Res*, *107*(D23, 4687), doi:10.1029/2002JD002054.

Ferrare, R. A., D. D. Turner, L. H. Brasseur, W. F. Feltz, O. Dubovik, and T. P. Tooman (2001), Raman lidar measurements of the aerosol extinction-to-backscatter ratio over the southern great plains, *J. Geophys. Res*, *106*, 20,333–20,348, doi: 10.1029/2000JD000144.

Gamage, N., and C. Hagelberg (1993), Detection and analysis of microfronts and associated coherent events using localized transforms, *J. Atmos. Sci.*, *50*(5), 750–756.

Hair, J. W., C. A. Hostetler, R. A. Ferrare, A. L. Cook, and D. B. Harper (2006), The nasa langley airborne high spectral resolution lidar for measurements of aerosols and clouds, in *Proceedings of 23rd International Laser Radar Conference (ILRC)*, edited by C. Nagasawa and N. Sugimoto, pp. 411–414.

Hegg, D. A., L. F. Radke, and P. V. Hobbs (1990), Particle production associated with marine clouds, *J. Geophys. Res*, *95*(D9), 13,917–13,926.

Hegg, D. A., D. S. Covert, H. Jonsson, D. Khelif, and C. A. Friehe (2004), Observations of the impact of cloud processing on aerosol light-scattering efficiency, *Tellus*, *56B*, 285–293.

Hoppel, W. A., G. M. Frick, J. W. Fitzgerald, and R. E. Larson (1994), Marine boundary layer measurements of new particle formation and the effects nonprecipitating clouds have on aerosol size distribution, *J. Geophys. Res*, *99*(D7), 14,443–14,459.

Ignatov, A., P. Minnis, N. Loeb, B. Wielicki, W. Miller, S. Sun-Mack, D. Tanre, L. Remer, I. Laszlo, and E. Geier (2005), Two MODIS aerosol products over ocean on the terra and aqua CERES SSF datasets, *J. Atmos. Sci.*, *62*, 1008–1031.

Kaufman, J. Y., I. Koren, L. A. Remer, D. Rosenfeld, and Y. Rudich (2005), The effect of smoke, dust, and pollution aerosol on shallow cloud development over the atlantic ocean, *Proc. Natl. Acad. Sci.*, *102*(32), 11,207–11,212.

Kerkweg, A., S. Wurzler, T. Reisin, and A. Bott (2003), On the cloud processing of aerosol particles: an entraining air-parcle model with two-dimensional spectral cloud microphysics and a new formulation of the collection kernel, *Quart. J. Roy. Meteorol. Soc.*, *129*(587), 1–18.

Koren, I., L. A. Remer, Y. J. Kaufman, Y. Rudich, and J. V. Martins (2007), On the twilight zone between clouds and aerosols, *Geophys. Res. Lett.*, *34*(L08805), doi: 10.1029/2007GL029253.

Lelieveld, J., and J. Heintzenberg (1992), Sulfate cooling effect on climate through in-cloud oxidation of anthropogenic SO2, *Science*, *258*, 117–120.

Loeb, N. G., and N. Manalo-Smith (2005), Top-of-atmosphere direct radiative effect of aerosols over global oceans from merged CERES and MODIS observations, *J. Climate*, *18*, 3506–3526.

Loeb, N. G., and G. L. Schuster (2008), An observational study of the relationship between cloud, aerosol and meteorology in broken low-level cloud conditions, *J. Geophys. Res*, *113*(accepted).

Marshak, A., G. Wen, J. A. C. Jr., L. A. Remer, N. G. Loeb, and R. F. Cahalan (2008), A simple model for the cloud adjacency effect and the apparent bluing of aerosols near clouds, *J. Geophys. Res, submitted.*

Matheson, M. A., J. A. C. Jr., and W. R. Tahnk (2005), Aerosol and cloud property relationships for summertime stratiform clouds in the northeastern atlantic from advanced very high resolution radiometer observations, *J. Geophys. Res*, *110*, doi: 10.1029/2005JD006165.

Matheson, M. A., J. A. C. Jr., and W. R. Tahnk (2006), Multiyear advance very high resolution radiometer observations of summertime stratocumulus collocated with aerosols in the northeastern atlantic, *J. Geophys. Res*, *111*(D15206), doi:10.1029/2005JD006890.

Mauger, G. S., and J. R. Norris (2007), Meteorological bias in satellite estimates of aerosol-cloud relationships, *Geophys. Res. Lett.*, *34*(L16824), doi:10.1029/2007GL029952.

Mitra, S. K., J. Brinkmann, and H. R.)ruppacher (1992), A wind tunnel study on the drop-to-particle conversion, *J. Aerosol Sci.*, *23*, 245–256.

O'Connor, E. J., A. J. Illingworth, and R. J. Hogan (2004), A technique for autocalibration of cloud lidar, *J. Atmos. Oceanic Technol.*, *21*, 777–786.

453 Pinnick, R. G., S. G. Jennings, P.Chylek, C. Ham, and W. T. G. Jr (1983), Backscatter
454 and extinction in water clouds, *J. Geophys. Res*, *88*, 6787–6796.

455 Podgorny, I. A. (2003), Three-dimensional radiative interactions in a polluted broken
456 cloud system, *Geophys. Res. Lett.*, *30*(14), 1771–1774, doi:10.1029/2003GL017287.

457 Remer, L. A., Y. Kaufman, D. Tanre, S. Mattoo, D. A. Chu, J. V. Martins, and coauthours
458 (2005), The MODIS aerosol algorithm, products, and validation, *J. Atmos. Sci.*, *62*,
459 947–973.

460 Schuster, G. L., O. Dubovik, and B. N. Holben (2006), Angstrom exponent and bimodal
461 aerosol size distributions, *J. Geophys. Res*, *111*(D07207), doi:10.1029/2005JD006328.

462 Sekiguchi, M., T. Nakajima, K. Suzuki, K. Kawamoto, A. Higurashi, D. Rosenfeld, I. Sano,
463 and S. Mukai (2003), A study of the direct and indirect effects of aerosols using global
464 satellite data sets of aerosol and cloud parameters, *J. Geophys. Res*, *108*(D22, 4699),
465 doi:10.1029/2002JD003359.

466 Tang, I. (1996), Chemical and size effects of hygroscopic aerosols on light scattering coef-
467 ficients, *J. Geophys. Res*, *101*(D14), 19,245–19,250.

468 Wen, G., A. Marshak, and R. F. Cahalan (2006), Impact of 3d clouds on clear sky re-
469 flectance and aerosol retrievals in biomass burning region of brazil, *Geosci. Remote*
470 *Sens. Lett.*, *3*, 169–172.

471 Wen, G., A. Marshak, R. F. Cahalan, L. A. Remer, and R. G. Kleidman (2007), 3-d
472 aerosol-cloud radiative interaction observed in collocated MODIS and ASTER images
473 of cumulus cloud fields, *J. Geophys. Res*, *112*(D13204), doi:10.1029/2006JD008267.

474 Wiscombe, W. (1980), Improved mie scattering algorithms, *Appl. Opt.*, *19*(9), 1505–1509.

Table 1. Estimated instantaneous uncertainties for HSRL observed variables at 532 nm: backscatter (β), extinction (σ), lidar ratio (S_a), depolarization (δ), backscatter Angstrom Exponent (BAE), and aerosol optical depth (AOD).

Variable	Uncertainty
$\beta(Mm^{-1}sr^{-1})$	0.36
$\sigma(km^{-1})$	0.055
$S_a(sr^{-1})$	14
δ	0.009
BAE	0.007
AOD	0.05

Table 2. Distances of the seven bins from the nearest clouds, and total number of samples of each bin for the three days.

Bin number	1	2	3	4	5	6	7
Distance (m)	1–500	501–1000	1001–1500	1501–2000	2001–3000	3001–4000	4001-5000
N (08/04)	37	29	24	20	26	27	25
N (08/07)	362	200	108	60	90	70	62
N (08/09)	246	120	75	52	55	25	24

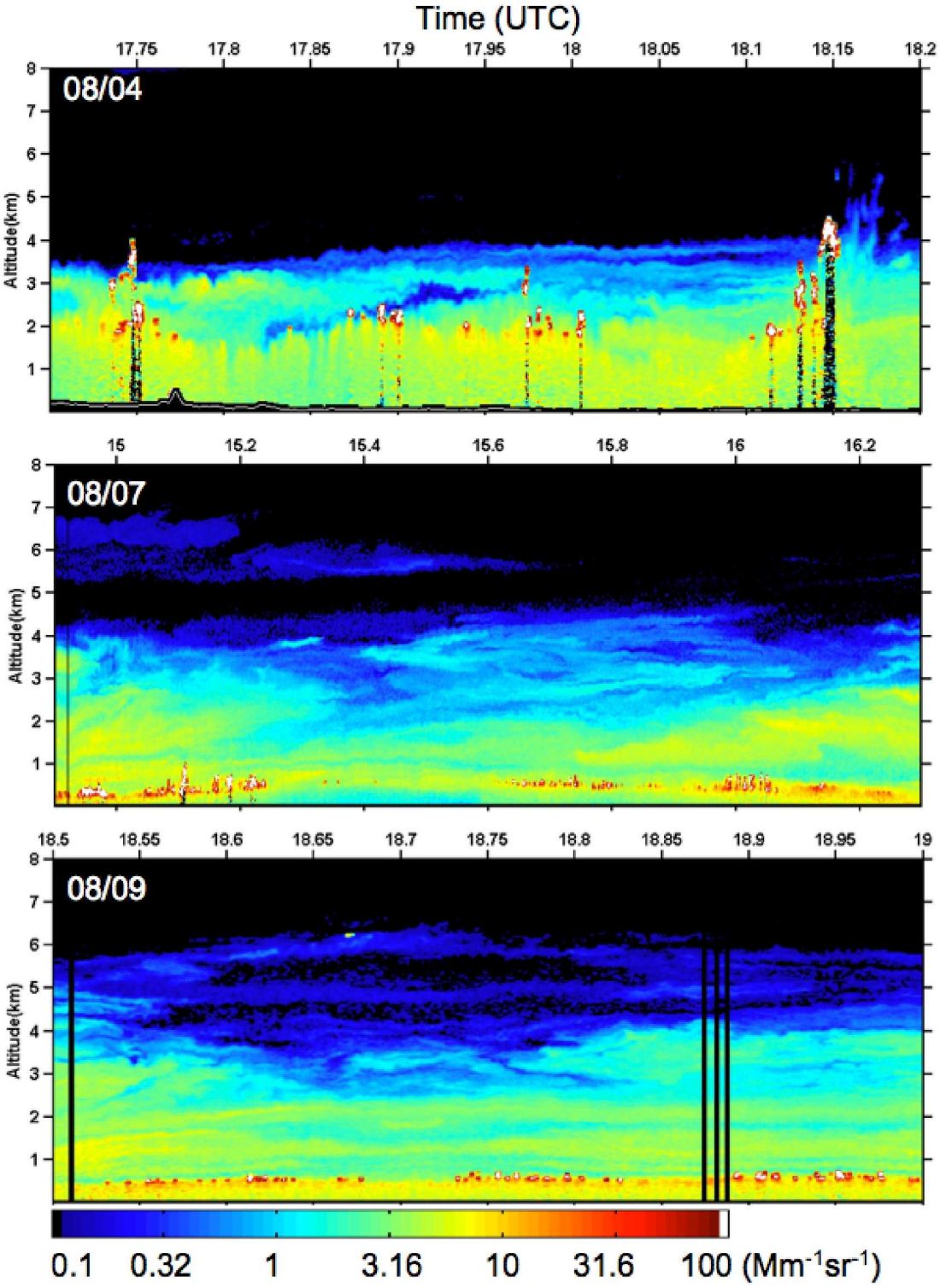

Figure 1. Backscatter coefficient profiles at 532 nm for the periods used in this analysis on August 4^{th}, 7^{th}, and 9^{th}, 2007.

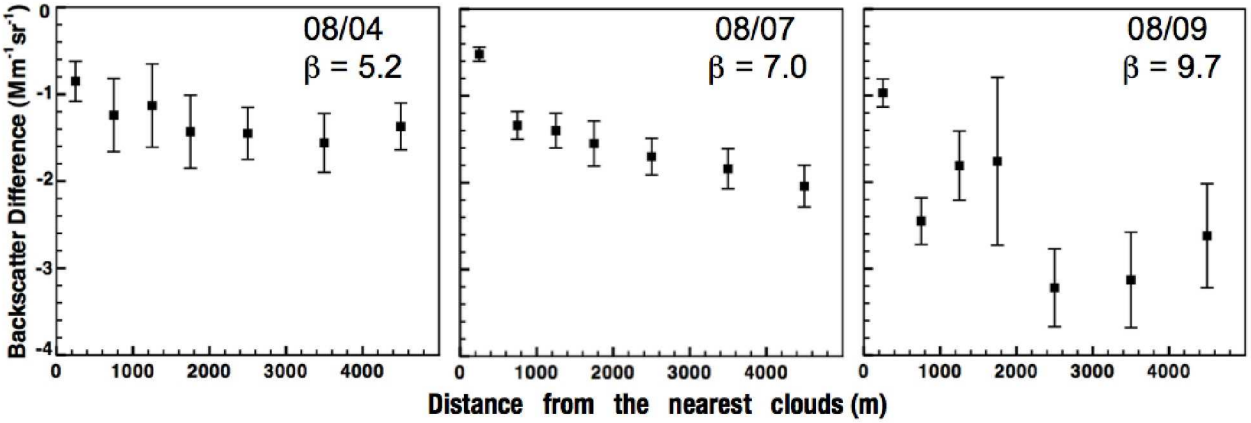

Figure 2. Average 532 nm backscatter differences ($\overline{\delta\beta}$) as a function of distance to nearest clouds on Aug. 4^{th}, 7^{th}, and 9^{th}, 2007. Error bar for each bin is the standard error of that bin, calculated as the standard deviation of the difference divided by the square root of the number of samples of that bin. Averaged near-cloud reference backscatter coefficients are also included in the figure. Negative differences indicate that far-cloud values are less than near-cloud values.

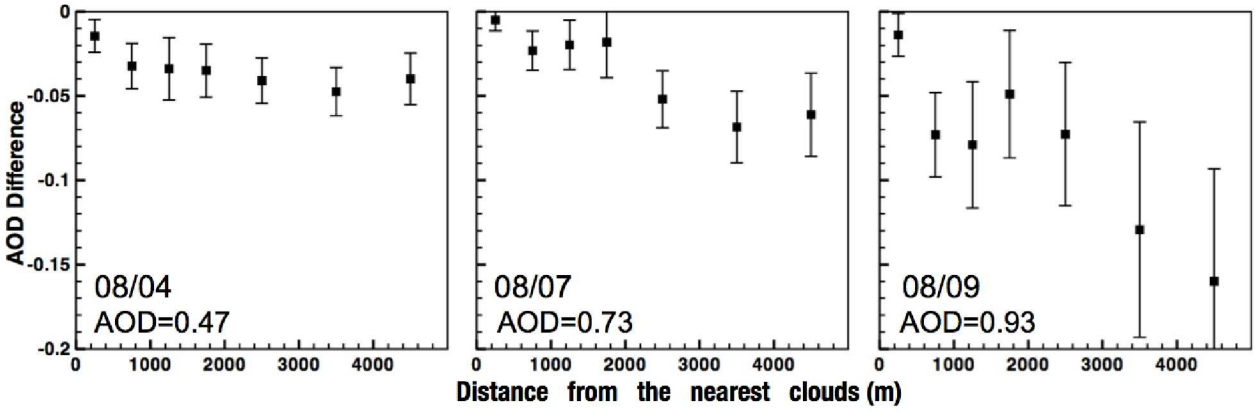

Figure 3. Average aerosol optical depth differences ($\overline{\delta AOD}$) as a function of distance to nearest cloud on Aug. 4^{th}, 7^{th}, and 9^{th}, 2007. Error bar stands for the standard error. Average near-cloud reference AODs are also included in the figure. Negative differences indicate that far-cloud values are less than near-cloud values.

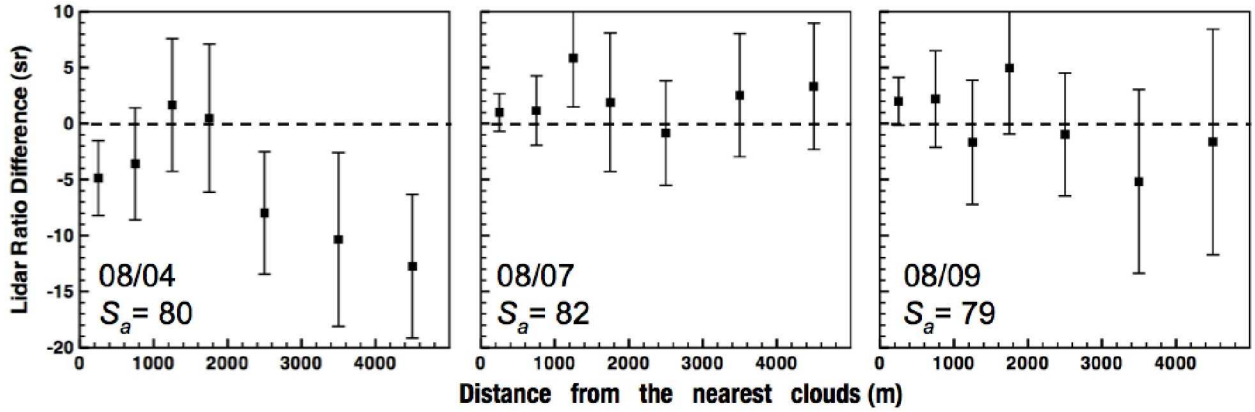

Figure 4. Average 532 nm lidar ratio differences ($\overline{\delta S_a}$) as a function of distance to nearest cloud on Aug. 4^{th}, 7^{th}, and 9^{th}, 2007. Error bar stands for the standard error. Average neaer-cloud reference lidar ratios are also included in the figure. Negative differences indicate that far-cloud values are less than near-cloud values.

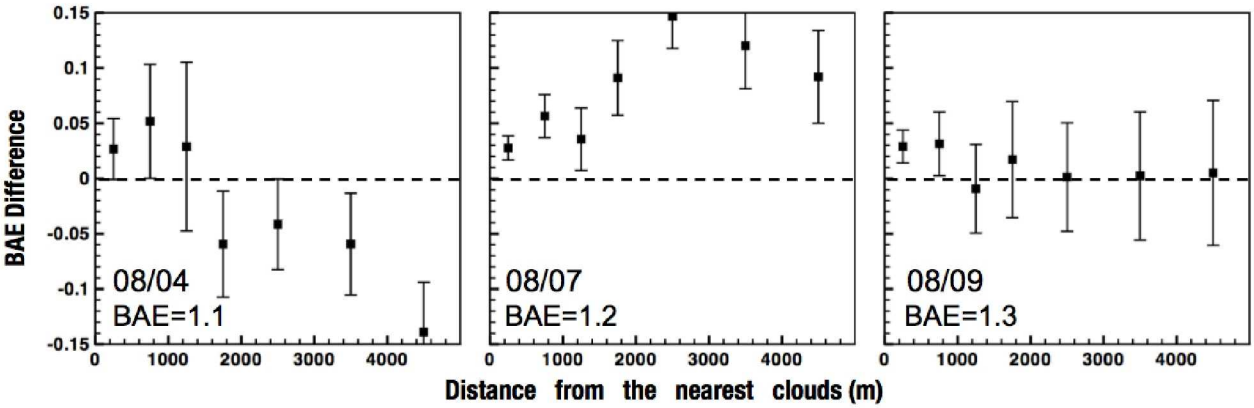

Figure 5. Average backscatter Angstrom exponent differences ($\overline{\delta BAE}$) as a function of distance to nearest cloud on Aug. 4^{th}, 7^{th}, and 9^{th}, 2007. Error bar stands for the standard error. Average near-cloud reference BAEs are also included in the figure. Negative differences indicate that far-cloud values are less than near-cloud values.

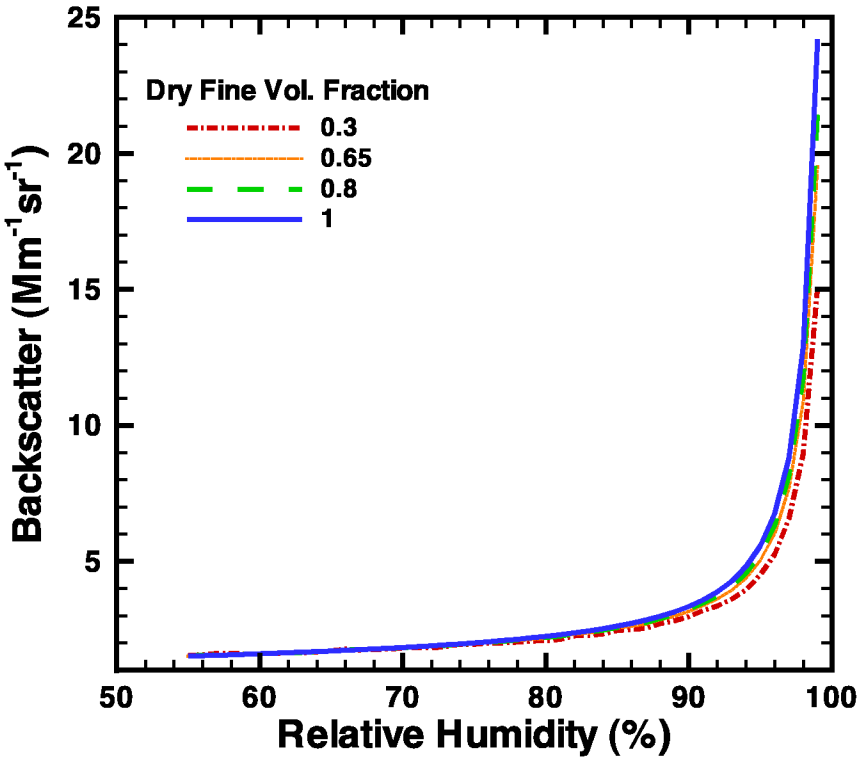

Figure 6. Backscatter coefficient as a function of relative humidity calculated using Mie theory based on GSFC climatology for four dry fine mode volume fractions. (Note that the wet fine volume fractions change along these curves.)

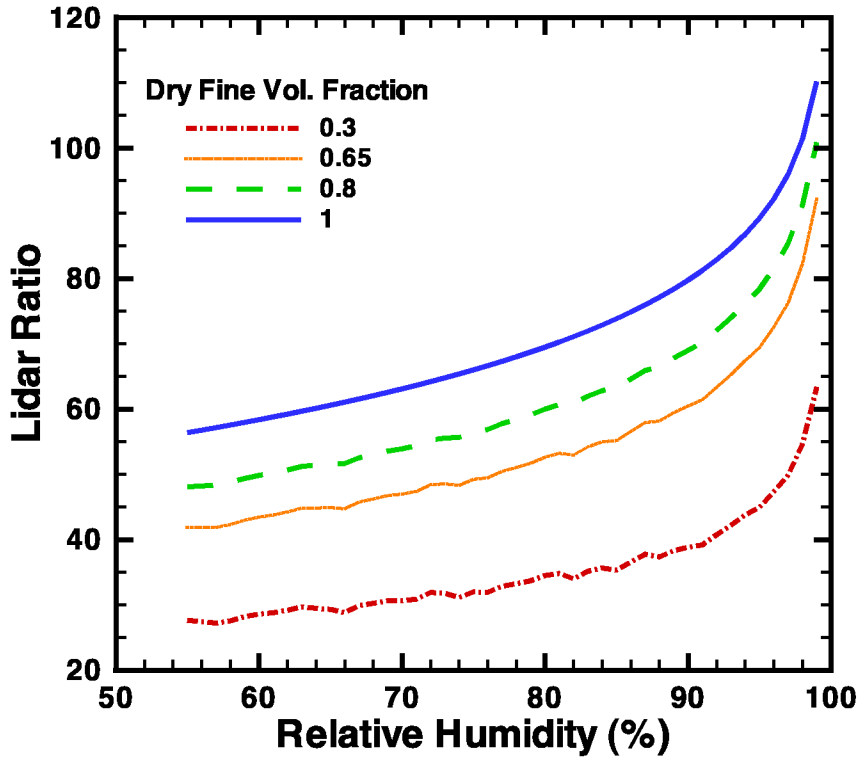

Figure 7. Lidar ratio as a function of relative humidity calculated using Mie theory based on GSFC climatology for four dry fine mode volume fractions.

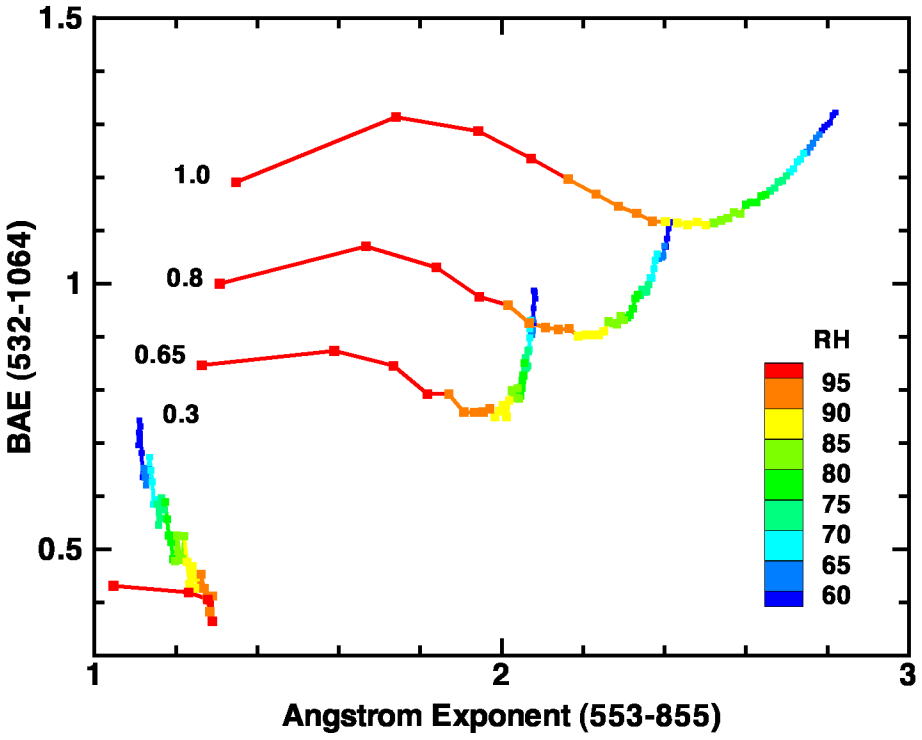

Figure 8. Relationship between backscatter Angstrom exponent for wavelength 532 nm and 1064 nm and Angstrom exponent for 553nm and 855 nm for four dry fine volume fractions as RH increases from 55% to 99%.